



## Helico-conical optical beams: a product of helical and conical phase fronts

Alonzo, C.A.; Rodrigo, P.J.; Glückstad, J.

*Published in:*  
Opt. Express

*Link to article, DOI:*  
[10.1364/OPEX.13.001749](https://doi.org/10.1364/OPEX.13.001749)

*Publication date:*  
2005

*Document Version*  
Publisher's PDF, also known as Version of record

[Link back to DTU Orbit](#)

*Citation (APA):*  
Alonzo, C. A., Rodrigo, P. J., & Glückstad, J. (2005). Helico-conical optical beams: a product of helical and conical phase fronts. *Opt. Express*, 13(5), 1749-1760. <https://doi.org/10.1364/OPEX.13.001749>

---

### General rights

Copyright and moral rights for the publications made accessible in the public portal are retained by the authors and/or other copyright owners and it is a condition of accessing publications that users recognise and abide by the legal requirements associated with these rights.

- Users may download and print one copy of any publication from the public portal for the purpose of private study or research.
- You may not further distribute the material or use it for any profit-making activity or commercial gain
- You may freely distribute the URL identifying the publication in the public portal

If you believe that this document breaches copyright please contact us providing details, and we will remove access to the work immediately and investigate your claim.

# Helico-conical optical beams: a product of helical and conical phase fronts

Carlo Amadeo Alonzo

National Institute of Physics, University of the Philippines, Diliman, Quezon City 1101, Philippines  
[ccalonzo@up.edu.ph](mailto:ccalonzo@up.edu.ph)

Peter John Rodrigo and Jesper Glückstad

Optics and Plasma Research Department, Risø National Laboratory, DK-4000 Roskilde, Denmark  
[jesper.gluckstad@risoe.dk](mailto:jesper.gluckstad@risoe.dk)

<http://www.ppo.dk>

**Abstract:** Helico-conical optical beams, different from higher-order Bessel beams, are generated with a parallel-aligned nematic liquid crystal spatial light modulator (SLM) by multiplying helical and conical phase functions leading to a nonseparable radial and azimuthal phase dependence. The intensity distributions of the focused beams are explored in two- and three-dimensions. In contrast to the ring shape formed by a focused optical vortex, a helico-conical beam produces a spiral intensity distribution at the focal plane. Simple scaling relationships are found between observed spiral geometry and initial phase distributions. Observations near the focal plane further reveal a cork-screw intensity distribution around the propagation axis. These light distributions, and variations upon them, may find use for optical trapping and manipulation of mesoscopic particles.

©2005 Optical Society of America

**OCIS codes:** (230.6120) Spatial light modulators, (050.1970) Diffractive optics (070.0070) Fourier optics and optical signal processing (140.7010) Trapping

---

## References and links

1. M. V. Berry, "Much ado about nothing: optical dislocation lines (phase singularities, zeros, vortices...)," in *Singular Optics*, M.S. Soskin, ed., Proc. SPIE **3487**, 1-5 (1998).
2. M.S. Soskin and M.V. Vasnetsov, "Singular Optics," in *Progress in Optics* **42**, E. Wolf, ed. (Elsevier, Amsterdam, 2001).
3. L. Allen, M.J. Padgett and M. Babiker, "The Orbital Angular Momentum of Light," in *Progress in Optics* **39**, E. Wolf, ed. (Elsevier, Amsterdam, 1999).
4. K. T. Gahagan and G. A. Swartzlander Jr., "Simultaneous trapping of low-index and high-index microparticles observed with an optical-vortex trap," J. Opt. Soc. Am. B **16**, 533-537 (1999).
5. P. J. Rodrigo, V. R. Daria and J. Glückstad, "Real-time interactive optical micromanipulation of a mixture of high- and low-index particles," Opt. Express **12**, 1417-1425 (2004), <http://www.opticsexpress.org/abstract.cfm?URI=OPEX-12-7-1417>.
6. V. R. Daria, P. J. Rodrigo and J. Glückstad, "Dynamic array of dark optical traps," Appl. Phys. Lett. **84**, 323-325 (2004).
7. N. B. Simpson, K. Dholakia, L. Allen and M. J. Padgett, "Mechanical equivalence of spin and orbital angular momentum of light: an optical spanner," Opt. Lett. **22**, 52-54 (1997).
8. J. E. Curtis and D. G. Grier, "Structure of optical vortices," Phys. Rev. Lett. **90**, 133901 (2003).
9. K. Ladavac and D. G. Grier, "Microoptomechanical pumps assembled and driven by holographic optical vortex arrays," Opt. Express **12**, 1144-1149 (2004), <http://www.opticsexpress.org/abstract.cfm?URI=OPEX-12-6-1144>.
10. P. A. Prentice, M. P. MacDonald, T. G. Frank, A. Cuschieri, G. C. Spalding, W. Sibbett, P. A. Campbell and K. Dholakia, "Manipulation and filtration of low-index particles with holographic Laguerre-Gaussian optical trap arrays," Opt. Express **12**, 593-600 (2004), <http://www.opticsexpress.org/abstract.cfm?URI=OPEX-12-4-593>.
11. M. J. Padgett and L. Allen, "The Poynting vector in Laguerre-Gaussian laser modes," Opt. Commun. **121**, 36-40 (1995).
12. J. A. Davis, E. Carcole and D. M. Cottrell, "Nondiffracting interference patterns generated with programmable spatial light modulators," Appl. Opt. **35**, 599-602 (1996).

13. N. Chattaripiban, E. A. Rogers, D. Cofield, W. T. Hill III and R. Roy, "Generation of nondiffracting Bessel beams by use of a spatial light modulator," *Opt. Lett.* **28**, 2183-2185 (2003).
14. N. R. Heckenberg, R. McDuff, C. P. Smith and A. G. White, "Generation of optical phase singularities by computer-generated holograms," *Opt. Lett.* **17**, 221-223 (1992).
15. M. W. Beijersbergen, L. Allen, H. E. L. O. van der Veen and J. P. Woerdman, "Astigmatic laser mode converters and transfer of orbital angular momentum," *Opt. Commun.* **96**, 123-132 (1993).
16. G.-H. Kim, J.-H. Jeon, K.-H. Ko, H.-J. Moon, J.-H. Lee and J.-S. Chang, "Optical vortices produced with a nonspiral phase plate," *Appl. Opt.* **36**, 8614-8621 (1997).
17. G. Biener, A. Niv, V. Kleiner and E. Hasman, "Formation of helical beams by use of Pancharatnam-Berry phase optical elements," *Opt. Lett.* **27**, 1875-1877 (2002).
18. C. Rotschild, S. Zommer, S. Moed, O. Hershcovitz and S. G. Lipson, "Adjustable spiral phase plate," *Appl. Opt.* **43**, 2397-2399 (2004).
19. K. Crabtree, J. A. Davis and I. Moreno, "Optical processing with vortex-producing lenses," *Appl. Opt.* **43**, 1360-1367 (2004).
20. M. V. Berry, "Optical vortices evolving from helicoidal integer and fractional phase steps," *J. Opt. A: Pure Appl. Opt.* **6**, 259-268 (2004).
21. J. Leach, E. Yao and M. J. Padgett, "Observation of the vortex structure of a non-integer vortex beam," *New J. Phys.* **6**, 71 (2004), <http://www.iop.org/EJ/abstract/1367-2630/6/1/071>.
22. S. H. Tao, W. M. Lee and X. Yuan, "Experimental study of holographic generation of fractional Bessel beams" *Appl. Opt.* **43**, 122-126 (2003).
23. J. W. Goodman, *Introduction to Fourier Optics*, Second Edition (McGraw-Hill, New York, 1996).
24. I. Moreno, C. Lemmi, A. Marquez, J. Campos and M. J. Yzuel, "Modulation light efficiency of diffractive lenses displayed in a restricted phase-mostly modulation display," *Appl. Opt.* **43**, 6278-6284 (2004).
25. O. Bryngdahl, "Geometrical transformations in optics," *J. Opt. Soc. Am.* **64**, 1092-1099 (1974).
26. J. Cederquist and A. M. Tai, "Computer-generated holograms for geometric transformations," *Appl. Opt.* **23**, 3099-3104 (1984).
27. J. E. Curtis and D. G. Grier, "Modulated optical vortices," *Opt. Lett.* **28**, 872-874 (2003).
28. J. Courtial, "Self-imaging beams and the Guoy effect," *Opt. Commun.* **151**, 1-4 (1998).

## 1. Introduction

The field of singular optics, in reference to light beams with phase singularities, has long been a fertile ground for both theoretical and applied research [1-3]. Such beams are most often referred to as optical vortices, a name evocative of the Poynting vector twisting about the phase singularity. An immediately striking trait of optical vortices is the vanishing field at the singularity location resulting in a doughnut- or ring-shaped intensity cross-section. One particular application that takes advantage of this intensity distribution is the trapping of particles with either high or low refractive indices using strongly focused optical vortices [4]. Although other techniques have also been demonstrated to generate ring-shaped optical traps [5,6], optical vortices carry an additional phenomenon of imparting an orbital angular momentum to the trapped particles [7,8]. These properties are seen as potentially useful in the development of optical microfluidic and micromanipulation systems [9,10].

There are several families of optical beams, such as Laguerre-Gaussian [11] and higher-order Bessel beams [12,13], that may be described as optical vortices. Common for them is a field distribution that features a complex exponential term,  $\exp(i\psi_\ell)$ , where the phase function is

$$\psi_\ell = \ell \theta. \quad (1)$$

Equation (1) describes a helix where the topological charge,  $\ell$ , is an integer that determines the number of  $2\pi$ -phase shifts that occur across one revolution of the azimuthal angle,  $\theta$ . The sign of  $\ell$  determines the handedness of the helix. While numerous methods are available to introduce a helical phase to an incident TEM<sub>00</sub> beam [12-18], the perhaps most convenient approach is to imprint the phase directly using a phase-only spatial light modulator (SLM) that emulates a helical phase plate [8]. The disadvantage of having to discretize the phase function is greatly offset by the ability to arbitrarily encode functions in two dimensions.

In general, aside from  $\psi_\ell$ , the optical beam may also have some radial phase dependence. For example, with the generation of higher-order Bessel beams the phase-carrying term can be written as  $\exp[i\psi(r,\theta)]$  with:

$$\psi(r,\theta) = \ell\theta - 2\pi r/r_o, \quad (2)$$

$r_o$  being a normalization factor of the radial coordinate,  $r$  [12]. Implications of combining the helical phase with the quadratic phase factor of a spherical lens have also been explored in the context of optical image processing [19]. However, previously considered mixed phase functions have usually been cast with separable radial and azimuthal dependence.

In this work, we implement a phase function with nonseparable dependence on  $r$  and  $\theta$ :

$$\psi(r,\theta) = \ell\theta(K - r/r_o), \quad (3)$$

where  $K$  is a constant that takes a value of either 1 or 0. In contrast to Eq. (2), which can be seen as a sum of a helical phase and a conical phase (such as from an axicon), Eq. (3) appears as a product of such functions. Consequently, the complex exponential cannot be separated into radial and azimuthal terms. We shall refer to Eq.(3) as a helico-conical phase, not to be confused with the phase in Eq. (2) for higher-order Bessel beams.

Aside from nonseparability, Eq. (3) also differs from Eqs. (1) and (2) in that it describes a phase that is not entirely continuous. The first two equations feature a phase steps of  $2\pi\ell$ , equivalent to a phase step of zero, for integral values of  $\ell$ . Interestingly, optical vortices with fractional values of  $\ell$ , *i.e.* discontinuous phase surfaces, have recently been described analytically [20] and demonstrated experimentally [21,22]. The phase described by Eq. (3), while similar to fractional optical vortices, differs further because the phase step varies linearly with  $r$  and the phase becomes continuous around an azimuthal circuit at  $r = r_o$ .

In this work, we examine the two-dimensional intensity distribution at the focal plane of a Fourier transforming lens illuminated by a plane wave encoded with a phase described by Eq. (3). Further, we show scaling relationships between the geometry of the intensity distribution and the initial parameters of the helico-conical beam. Intensity distributions at defocused planes are also explored to create a three-dimensional picture of the light distribution near the focus. These distributions are seen to be novel in comparison to those generated by previously considered radial and azimuthal phase functions.

## 2. Experiment setup

Figure 1 depicts the experimental apparatus used to generate beams with the desired phase function. The light source is a 30-mW HeNe laser ( $\lambda = 632.8$  nm) expanded to ~24-mm in diameter by a Keplerian beam expander (L1, L2) fitted with a pinhole spatial filter (PH). The intensity of the beam is controlled with a  $\lambda/2$ -retarder (HP) and Glan-laser polarizer (GL) tandem. For compactness, the expanded beam is passed through a beam splitter (BS) onto the 20 x 20 mm face of a reflection-type spatial light modulator (SLM; Hamamatsu Photonics X7550). An adjustable circular aperture stop (CA) with a maximum diameter of 11 mm is placed in front of the SLM surface. The BS directs reflected light from the SLM towards a CCD camera mounted with a neutral density filter (ND). A 200-mm focal length lens (L3) is placed in a 2- $f$  configuration with the SLM and CCD at the front and back focal planes, respectively. Video and images are captured from the CCD by a personal computer through a PCI video capture card.

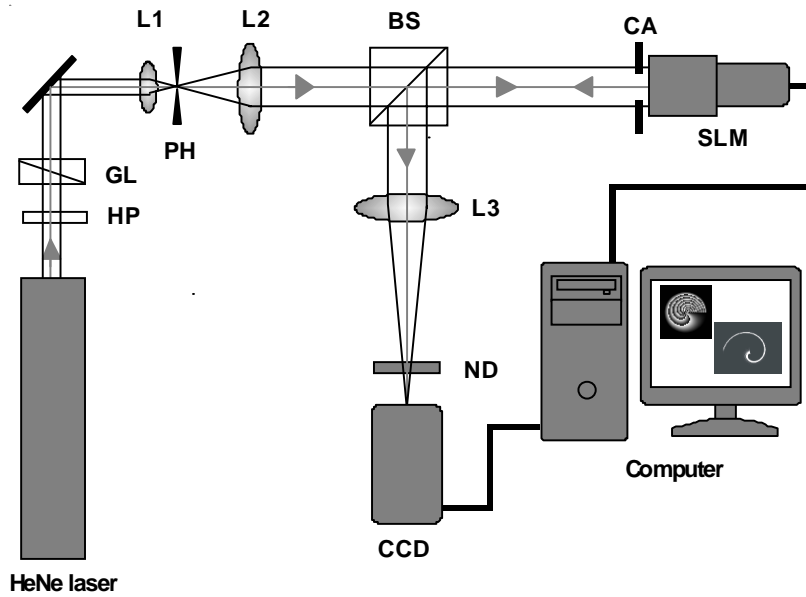


Fig. 1. Setup for generation of phase-encoded beams and corresponding Fourier transforms.

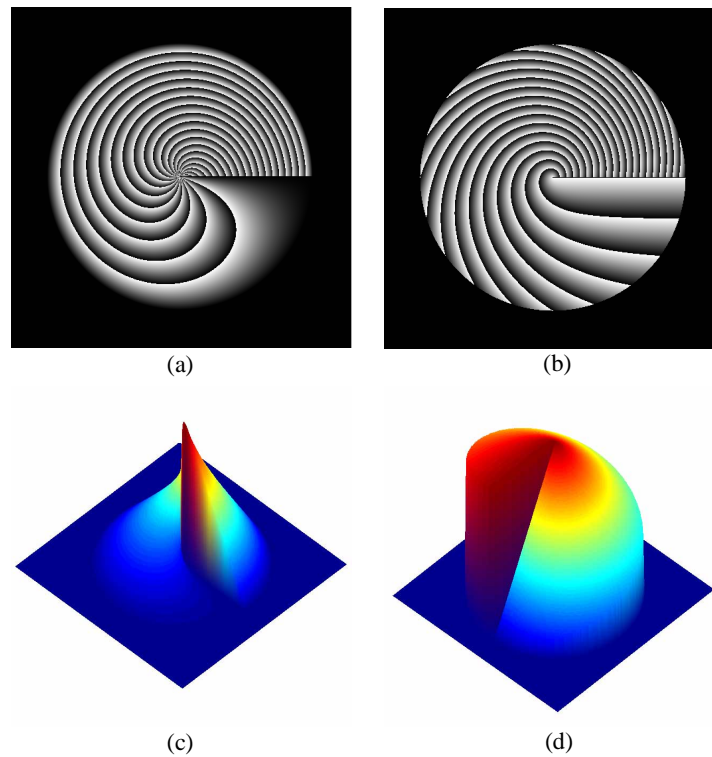


Fig. 2. Typical phase masks encoded onto the SLM with (a)  $K = 1$ , (b)  $K = 0$ . Lighter gray-level indicates greater phase. In pseudo-color unwrapped representation in (c)  $K = 1$  and (d)  $K = 0$ , red has highest phase while blue has lowest.

Given linearly polarized light properly oriented with respect to the parallel-aligned nematic liquid crystals, the SLM can perform phase-only modulation from 0 to  $\sim 2\pi$  in 230 discrete steps. The  $480 \times 480$  array of  $40\text{-}\mu\text{m}$  pixels are optically addressed to minimize dead-space on the SLM surface. Phase masks are drawn as grey-level images on a personal computer and directed via the VGA output to the SLM. Typical images used as phase masks are presented in Fig. 2(a) and Fig. 2(b) corresponding to Eq. (3) with  $K=1$  and  $K=0$ , respectively.  $r_o$  is chosen to coincide with the radius of CA. Note that the encoded phases are wrapped in  $2\pi$ . Figures 2(c) and 2(d) show the mixed helical and conical shapes of the corresponding unwrapped phase profiles.

### 3. Intensity distribution at the focal plane

Scalar diffraction theory relates the field distributions at the front and back focal plane of a spherical lens by a Fourier transform. The intensity measured at the CCD sensor is then given by  $I(\rho, \phi) = |u(\rho, \phi)|^2$  with

$$u(\rho, \phi) = \int_0^{2\pi} \int_0^\infty \text{circ}(r/r_o) \exp[i\psi(r, \theta)] \exp[-i2\pi\rho \cos(\theta - \phi)] r dr d\theta. \quad (4)$$

$\text{circ}(r/r_o)$  is the *Circle* function [23] used to describe the circular aperture stop, and  $\psi(r, \theta)$  is defined as in Eq. (3). For simplicity, we assume that the area of the expanded Gaussian beam enclosed by radius  $r_o$  can be approximated by a plane wave. As emphasized earlier, because of the chosen form of  $\psi(r, \theta)$ , the double integral is not separable in  $r$  and  $\theta$ . It is thus most convenient to evaluate Eq. (4) numerically with an FFT algorithm.

Figures 3(a) and 3(b) compare an actual image captured on the CCD camera with a numerical result for  $K=1$ . The strong correspondence between numerical and experimental results is emphasized by the composite image in Fig. 3(c). The intensity distribution at the focal plane appears quite distinctly as a spiral, specifically an arithmetic spiral of points with radial position,  $\rho_\phi$ , proportional to azimuthal angle,  $\phi$ . An arithmetic spiral,  $\rho_\phi = 0.13\phi$ , is superimposed on the results in Fig. 3(c) to highlight the basic geometry of the intensity distribution.

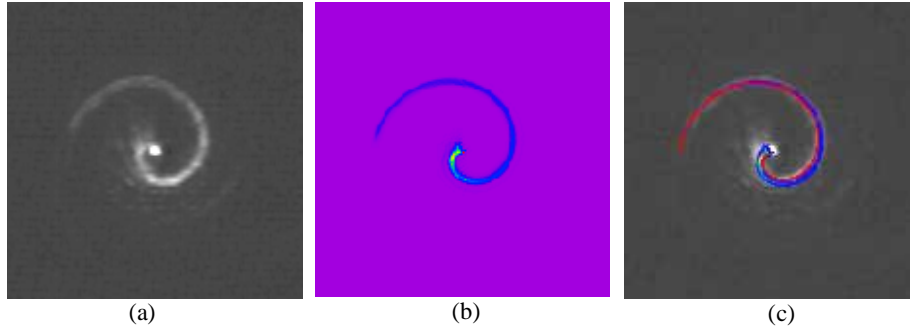


Fig. 3. Intensity distribution at the focal plane with  $K=1$ . (a) image captured from CCD, increasing intensity from black to white; (b) numerical simulation, increasing intensity from violet to red; (c) a simple arithmetic spiral is superimposed in red, on top of the numerical simulation in pseudo-color, and the captured image in gray-scale.

The observed spiral pattern brings to mind the broken-ring intensity distribution associated with fractional optical vortices [20-22]. One might then also expect to find a chain of alternating-sign vortices embedded in the dark regions of the field distribution. Locations of these vortices could be mapped by investigating the phase structure of the propagated beams

as in [20,21]. In this work, however, we shall limit our discussion to explorations of the intensity distributions.

An arithmetic spiral in the focal plane is not a surprising result if the phase function as depicted in Fig. 2(a) is considered with some detail. We may look at the two-dimensional distribution as a superposition of one-dimensional radial segments. Each individual segment appears as a blazed grating with a constant slope

$$m_\theta = \ell\theta/r_o. \quad (5)$$

The slope then increases proportionally to the azimuthal position of the segment. A plane wave incident on a particular segment will be deflected to a point on the Fourier plane corresponding to a spatial frequency proportional to  $m_\theta$ . Accumulating the contributions from each segment around the azimuthal angle thus draws an arithmetic spiral on the Fourier plane. Moreover, following Eq. (5), we would expect this spiral to scale linearly with  $\ell/r_o$ . We shall explore this point further later.

Following a similar analysis, we find that the phase distribution for  $K=0$  may also be decomposed into radial segments with slopes  $m_\theta$ . We might then expect the intensity distribution to be the same as in the previous case. Figures 4(a) and 4(b) however, are clearly different from Figs. 3(a) and 3(b). The most obvious point is an intensity peak forming a compact head on the spiral that is displaced from the origin of the Fourier plane when  $K=0$ . Figure 4(c) also reveals that, close to the origin, the intensity distribution deviates from an arithmetic spiral drawn in red.

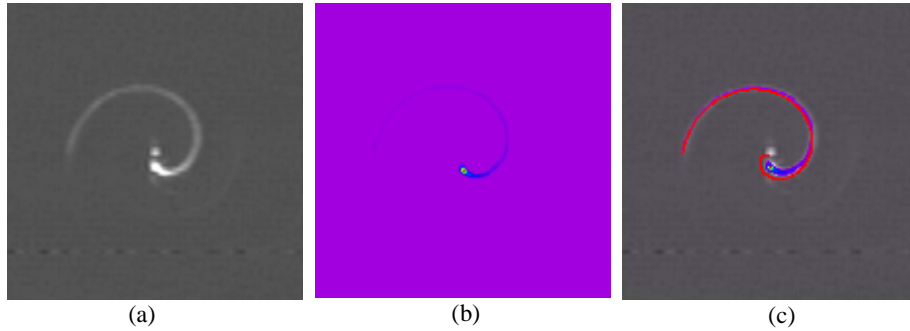


Fig. 4. Intensity distribution at the focal plane with  $K=0$ . (a) image captured from CCD; (b) numerical simulation; (c) a simple arithmetic spiral is superimposed in red, on top of the numerical simulation in pseudo-color, and the captured image in gray-scale.

To resolve this discrepancy, we return to the case of  $K=1$ . The complete phase function across a single radial segment as earlier considered is

$$\psi_{K=1} = \ell\theta - m_\theta r. \quad (6)$$

If we compare the equivalent expression for  $K=0$ ,

$$\psi_{K=0} = -m_\theta r, \quad (7)$$

the difference is the first term in Eq. (6). Bearing in my mind that  $\ell\theta$  is constant within each radial segment but varies between segments, it effectively introduces an azimuthally varying phase-offset in  $\psi_{K=1}$  that is not present in  $\psi_{K=0}$ . We then interpret the results Figs. 4(a) and 4(b) as indicating that the coherent superposition of diffracted waves from each segment interfere destructively close to the origin when  $K=0$ . When  $K=1$ , such coherent superposition is compromised by relative phase shifts,  $\ell\theta$ , between radial segments, leading to a fully formed arithmetic spiral at the focal plane.

At this point, we comment on the central maximum displayed on the captured image in Fig. 4(a), but not present in the numerical calculation, Fig. 4(b). This zero-order diffraction is easily accounted for in the simulation when the realistic modulation range of the SLM is considered. Actual phase modulation of the SLM does not reach  $2\pi$  for the wavelength used (632.8 nm), but peaks at  $1.8\pi$ . Such limitations can be mitigated by techniques that map the initial phase function to a projection optimal for the limited range of the device [24]. However, dead-space on the SLM, as well as multiple reflections from the beam splitter cube, would still contribute to a bright spot at the focus.

The addition of a carrier wave to the object phase is a common technique used to isolate the desired first-order diffraction from the zero-order and other components [21]. However, this increases the space-bandwidth product (SBP) required to render the same image on the SLM. The limited SBP available will result in aliasing issues as more rapidly varying phase functions, *i.e.* large  $\ell/r_o$  -values, are encoded.

We also observed an increased visibility of higher diffraction orders with more rapidly varying phase functions. We attribute this result to edge bleeding in the optically-addressed SLM. This limitation in rendering high contrast edge features, such as phase steps, leads to the unwanted diffraction of light towards other orders. Figure 5 illustrates this problem using the optical Fourier transform of a simple linear blazed grating. Although the desired (positive) first-order is clearly projected, some light is diffracted to (negative) higher-orders on the opposite side. The undesired orders are lower in intensity and may be suppressed by reducing the overall illumination, however the amount of misdirected light increases when the encoded phase mask contains more phase steps.



Fig. 5. Diffraction from a linear blazed grating encoded on the SLM. The experimentally obtained diffraction orders are labeled as -3, -2, -1, 0, and 1, respectively.

#### 4. Analysis by local spatial frequency

A more formal analysis, compared to the above interpretation of the observed spiral intensity distributions, is provided by utilizing the concept of local spatial frequency [23]. In rectangular coordinates, the Fourier transform,

$$G(\xi, \zeta) = \int_{-\infty}^{\infty} \int_{-\infty}^{\infty} g(x, y) \exp[-i2\pi(\xi x + \zeta y)] dx dy, \quad (8)$$

of an object function,

$$g(x, y) = a(x, y) \exp[i\bar{\psi}(x, y)], \quad (9)$$

can be seen as a superposition of plane waves with spatial frequency components,  $(\xi, \zeta)$ . Strictly speaking, frequency components at the Fourier plane cannot be associated to particular spatial coordinates in the front focal plane. However, for an object field with slowly varying amplitude,  $a(x, y)$ , and phase,  $\bar{\psi}(x, y)$ , functions, an approximate mapping can be provided by local spatial frequencies defined as



$$\xi' = \frac{1}{2\pi} \frac{\partial}{\partial x} \bar{\psi}(x, y) \quad \text{and} \quad \zeta' = \frac{1}{2\pi} \frac{\partial}{\partial y} \bar{\psi}(x, y). \quad (10)$$

Equation (10) can be arrived at by solving the Fourier integral by the method of stationary phase [25,26].

A previous work presents a similar approach to manipulate the intensity distributions of optical vortex traps [27]. By assuming a mapping based on  $\partial\psi/\partial\theta$ , the radius of a focused optical vortex is modulated into various Lissajous curves while still imparting orbital angular momentum to trapped particles. Local spatial frequency analysis possibly provides a basis for the observed pattern modulation.

Applying Eq. (10) to our phase function defined in Eq. (3) in rectangular coordinates, and transforming back to polar coordinates, for  $K=1$  we arrive at

$$\xi' = \frac{\ell}{2\pi r_o} \left[ -\theta \cos \theta - \left( \frac{r_o - r}{r} \right) \sin \theta \right] \quad \text{and} \quad \zeta' = \frac{\ell}{2\pi r_o} \left[ -\theta \sin \theta + \left( \frac{r_o - r}{r} \right) \cos \theta \right]. \quad (11)$$

Figure 6(a) plots  $(\xi', \zeta')$  as a spot diagram following Eq. (11). The density of points is representative of intensity observable at the focal plane. In the figure, we observe that some points have accumulated in a spiral. The local spatial frequencies forming the spiral appear to be associated with points on the object plane closest to the circular boundary. Taking the limit as  $r \rightarrow r_o$ , we find  $\rho_\phi = (\xi'^2 + \zeta'^2)^{1/2} \rightarrow \frac{1}{2\pi} \frac{\ell \theta}{r_o}$  and  $\phi = \tan^{-1}(\zeta'/\xi') \rightarrow \theta$ . The dense collection of points thus forms an arithmetic spiral on the focal plane that scales linearly with  $\ell/r_o$ , as suggested earlier by Eq. (5).

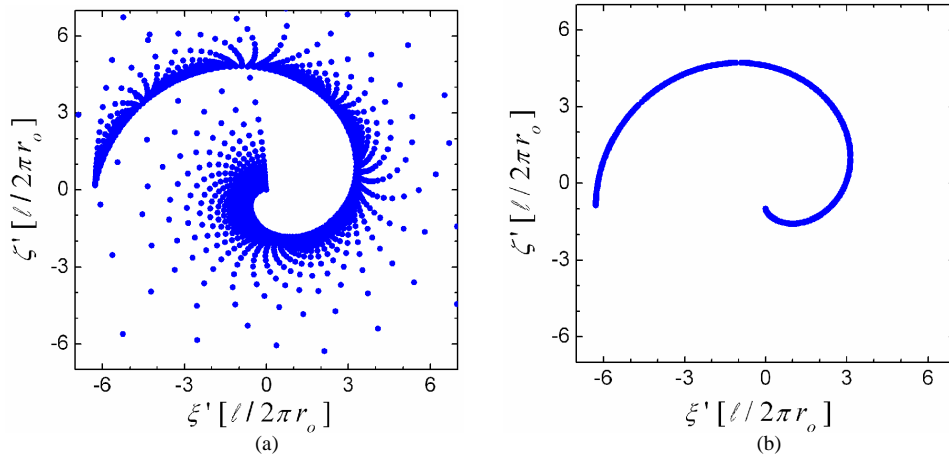


Fig. 6. Spot diagram of local spatial frequencies  $(\xi', \zeta')$  for (a)  $K=1$ , and (b)  $K=0$ . Density of plotted points approximately corresponds to observable intensity on the focal plane.

Similar analysis for the case of  $K=0$  yields

$$\xi' = \frac{\ell}{2\pi r_o} [-\theta \cos \theta + \sin \theta] \quad \text{and} \quad \zeta' = \frac{\ell}{2\pi r_o} [-\theta \sin \theta - \cos \theta]. \quad (12)$$

A notable feature of Eq. (12) is the lack of dependence on  $r$ . This results in a very compact distribution of points into a spiral as shown in Fig. 6(b), and an observable dislocation of the spiral's head from the origin of the focal plane as opposed to when  $K=1$ . In agreement with

results from the numerical simulation and experiment in Fig. 4(c), Eq. (12) does not yield a strictly arithmetic spiral. Further, the resulting pattern also scales linearly with  $\ell/r_o$ .

Scaling with  $1/r_o$  may also be inferred from the *similarity theorem* of Fourier transforms [23]. A normalization of radial coordinates in the input plane,  $r/r_o$ , translates to an expansion of radial coordinates in the Fourier plane,  $r_o\rho$ . Scaling with  $\ell$  is seen as analogous to the scaling behavior observed between optical vortices and their corresponding topological charge [8]. Figures 7(a) and 7(b) confirm the experimental observation of linear  $\ell/r_o$ -scaling.  $\rho_\phi$  is measured along  $\phi = \pi$  on images generated with varying permutations of  $\ell$  (5, 10, 20, 40, 60, 80, and 100) and  $r_o$  (3.0 mm, 4.5 mm, and 5.5 mm).

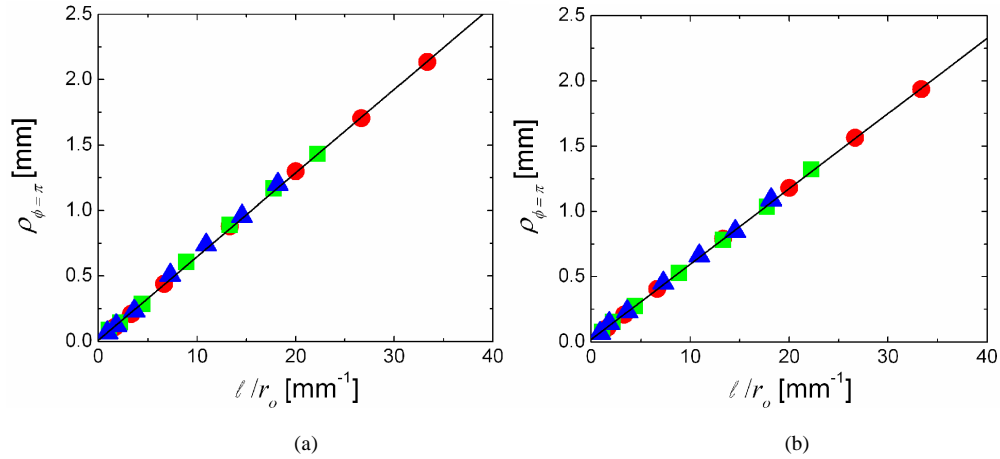


Fig. 7. Linear scaling of spirals at the focal with (a)  $K = 1$  and (b)  $K = 0$ . Radial distances from the origin were measured at  $\phi = \pi$ . Phase functions encoded onto SLM used  $\ell$ -values ranging from 5 to 100, and  $r_o$ -values of 3.0 mm (red circles), 4.5 mm (green squares), and 5.5 mm (blue triangles).

### 5. Three-dimensional intensity distribution near the focal plane

Moving the CCD camera away from the focal plane allows us to visualize the nearby propagation of the focused helico-conical beams. The intensity distribution in this region was also calculated using Fresnel propagation of the complex fields from the focal plane.  $u(\rho, \phi)$  is decomposed into plane wave components by a Fourier transform, then multiplied by the quadratic phase factor associated with free-space propagation for a distance,  $z$ . An inverse Fourier transform of the result yields the desired distribution at the defocused plane. Intensity values extracted from these field distributions for different  $z$  are stacked to form a three-dimensional representation of the light distribution near the focal plane.

Figure 8 presents the captured intensity distributions for  $K = 1$ . There is a stark contrast in the propagation dynamics for  $z < 0$  (approaching the focal plane) and  $z > 0$  (beyond the focal plane). An interesting feature for  $z < 0$  is the apparent rotation of the intensity profile as the beam propagates towards the focal plane. The irregular-spiral intensity pattern also appears to reverse in handedness as it evolves in the region prior to the focal plane. Propagation for  $z > 0$ , meanwhile, is dominantly characterized by a dilation of the intensity distribution from the focal plane and remains nearly invariant in structure. These phenomena are seen more clearly with the pseudo-color representation of the numerical results in Fig. 9. It is perhaps worth noting that the propagation dynamics are reversed when the conjugate phase functions are considered, for example if  $\ell$  is chosen to be negative.

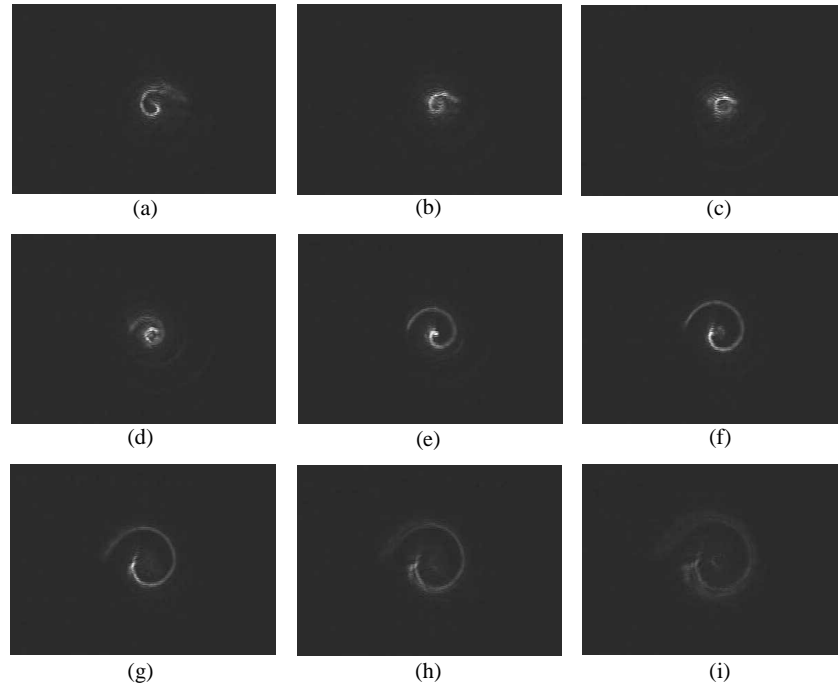


Fig. 8. (AVI, 1.067 MB) Propagation of focused beam with  $K = 1$ . Images (a) through (i) cover a total distance of  $\sim 40$  mm, with (a) being closest to the lens, and (e) at the focal plane.

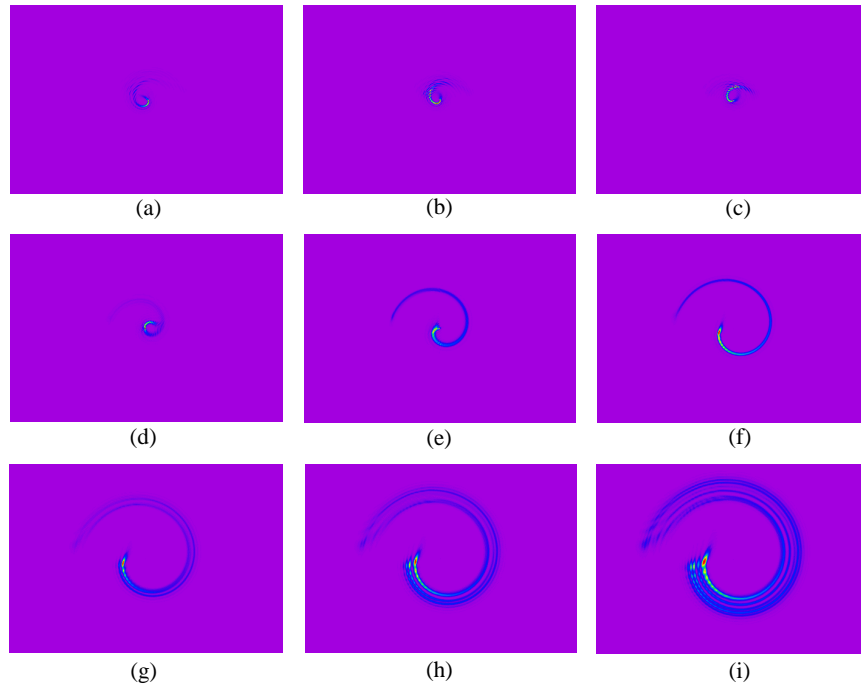


Fig. 9. (animated GIF, 261 kB) Numerical simulation of focused beam propagation with  $K = 1$ . Distances from focal plane used to calculate images are (a) -20 mm, (b) -16 mm, (c) -12 mm, (d) -6 mm, (e) 0 mm, (f) 6 mm, (g) 12 mm, (h) 16 mm, and (i) 20 mm.

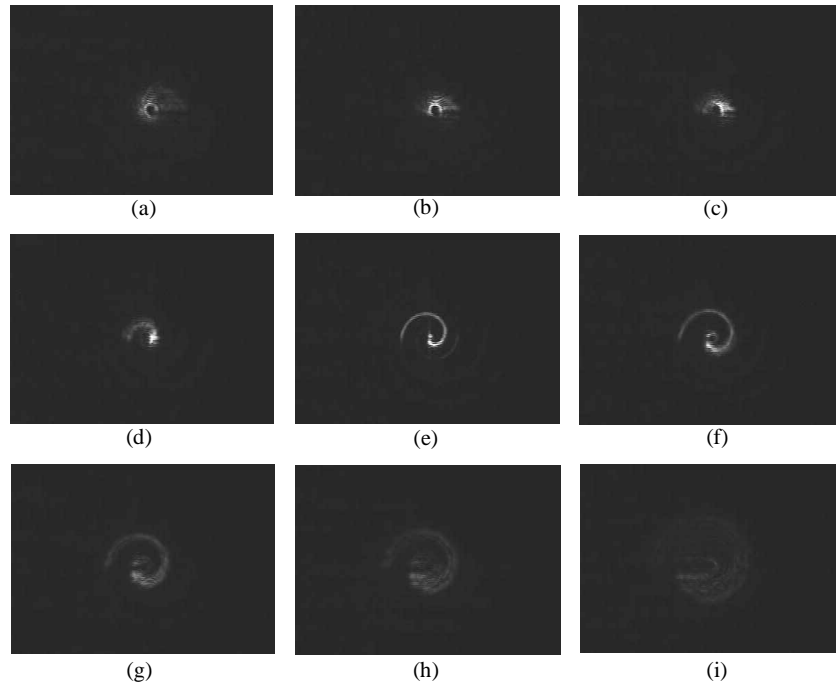


Fig. 10. (AVI, 1.01 MB) Propagation of focused beam with  $K = 0$ . Images (a) through (i) cover a total distance of  $\sim 40$  mm, with (a) being closest to the lens, and (e) at the focal plane.

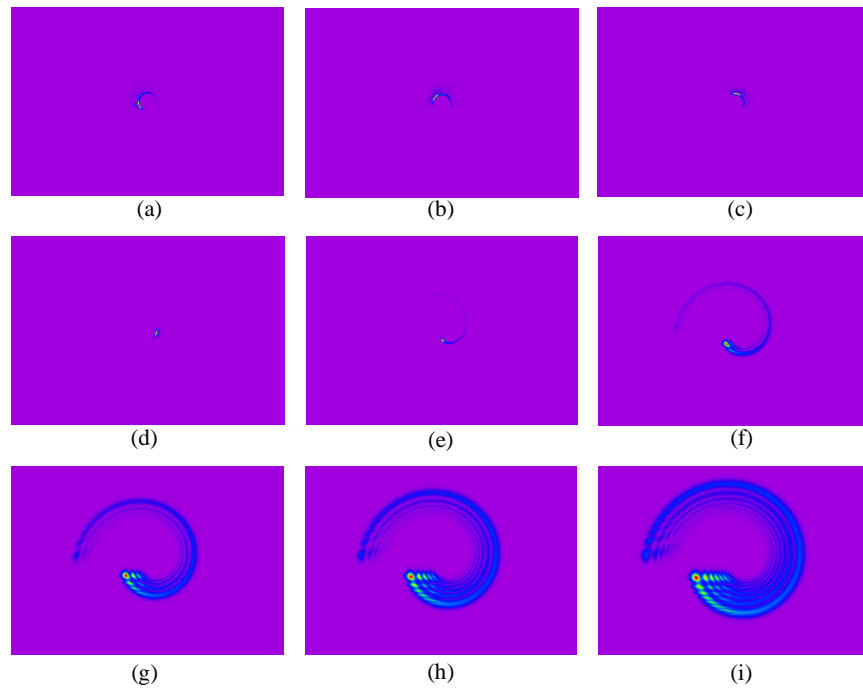


Fig. 11. (animated GIF, 275 kB) Numerical simulation of focused beam propagation with  $K = 0$ . Distances from focal plane used to calculate images are (a) -20 mm, (b) -16 mm, (c) -12 mm, (d) -6 mm, (e) 0 mm, (f) 6 mm, (g) 12 mm, (h) 16 mm, and (i) 20 mm.

Similar propagation dynamics are observed in Fig. 10 for  $K = 0$ . Rotation of the intensity profile, simultaneous with a switching in the direction of the tail of the spiral, is observed while approaching the focus. This, again, is followed by dilation of the intensity pattern beyond the focal plane. However, the particular intensity profile projected by the phase distribution when  $K = 0$  leads to a more interesting dynamics in the region  $z < 0$ . Following the intensity profile carefully, we can observe that the head of the spiral follows a cork-screw path around the optical axis. Again, the use of a pseudo-color representation more prominently presents this behavior with the numerical results in Fig. 11. With sufficiently intense input illumination, one could imagine particles being guided along the path of this intensity “hot spot”.

Projection of the initial phase function onto a basis set of component modes, particularly the Laguerre-Gaussian (LG) modes, may provide some insights on the underlying dynamics behind the evolution of observed intensity distributions in the propagating beam [28]. Unfortunately, the lack of structural stability or self-imaging properties in the beam suggests that the decomposition will be non-trivial. Further, numerical simulations did not reveal any obvious association between prominent propagation features, *i.e.* the rotation and the switching of handedness by the intensity patterns, with either the Rayleigh range ( $z_R$ ), or the Gouy phase shift ( $\arctan(z/z_R)$ ). The latter in particular is a key parameter in the propagation of LG modes. This result would also suggest a large set of LG component modes forming the helico-conical beams.

## 6. Conclusion

We introduced, in Eq. (3), a phase distribution with nonseparable radial and azimuthal dependence that results from the product of a helical and conical phase fronts, and generates helico-conical beams, different from the higher-order Bessel beams. Rather than forming the ring-shaped intensity distributions characteristic of optical vortices, focusing these beams produces spiral intensity distributions at the focal plane. An interpretation of the observed distributions in terms of the superposition of radially arranged, linear blazed-gratings was initially presented, followed by a more formal analysis by local spatial frequencies. The spiral profiles were shown to scale linearly with the initial parameters,  $\ell/r_o$ , of the encoded phase profiles.

Observations at defocused planes revealed a strong asymmetry of the propagation dynamics with respect to the focal plane. A rotation of intensity distributions was observed when approaching the focal plane, while moving beyond the focal plane led principally to dilation of the intensity patterns. Propagation towards the focal plane was seen to be particularly interesting when  $K = 0$ , where the projected intensity distribution forms an intensity hot spot that follows a cork-screw path around the propagation axis.

Although the behavior of particles trapped by these beams focused with a high NA remains to be seen, the actions of a non-symmetric beam possessing orbital angular momentum is an enticing prospect. Its potential application might include rotational positioning of asymmetric particles, or even the collection and accumulation of smaller particles towards the focus.